# Rainforest-initiated wet season onset over the southern Amazon

Jonathon S. Wright[a], Rong Fu[b,1], John R. Worden[c], Sudip Chakraborty[b], Nicholas E. Clinton[d], Camille Risi[e], Ying Sun[c,2], and Lei Yin[f]

[a]Department of Earth System Science, Tsinghua University, Beijing 100084, China; [b]Department of Atmospheric and Oceanic Sciences, University of California, Los Angeles, CA 90095; [c]Jet Propulsion Laboratory, California Institute of Technology, Pasadena, CA 91109; [d]Geo for Good, Google, Inc., Mountain View, CA 94043; [e]Laboratoire de Météorologie Dynamique, Institut Pierre Simon Laplace, 75252 Paris, France; and [f]Jackson School of Geosciences, University of Texas at Austin, Austin, TX 78712

Edited by Mark H. Thiemens, University of California at San Diego, La Jolla, CA, and approved June 14, 2017 (received for review January 3, 2017)

**Although it is well established that transpiration contributes much of the water for rainfall over Amazonia, it remains unclear whether transpiration helps to drive or merely responds to the seasonal cycle of rainfall. Here, we use multiple independent satellite datasets to show that rainforest transpiration enables an increase of shallow convection that moistens and destabilizes the atmosphere during the initial stages of the dry-to-wet season transition. This shallow convection moisture pump (SCMP) preconditions the atmosphere at the regional scale for a rapid increase in rain-bearing deep convection, which in turn drives moisture convergence and wet season onset 2–3 mo before the arrival of the Intertropical Convergence Zone (ITCZ). Aerosols produced by late dry season biomass burning may alter the efficiency of the SCMP. Our results highlight the mechanisms by which interactions among land surface processes, atmospheric convection, and biomass burning may alter the timing of wet season onset and provide a mechanistic framework for understanding how deforestation extends the dry season and enhances regional vulnerability to drought.**

rainfall | rainforest | Amazon | evapotranspiration | monsoon onset

The southern Amazon, which covers ∼30–40% of Amazonia, is a transitional region between tropical rainforests to the north and west and subtropical savanna and agricultural lands to the south and east (Fig. 1). Rainforests in this region, which play an important role in the global carbon cycle (1), are vulnerable to slight decreases in annual rainfall or increases in dry season length (2). This vulnerability is exacerbated by large-scale agricultural land use. The southern Amazon dry season has lengthened in recent decades, primarily due to delays in wet season onset (3). Model simulations suggest that continuation of this trend could trigger an abrupt transition of rainforest to savanna (2, 4), which would substantially reduce dry season rainfall over the southern Amazon and downwind agricultural regions (5, 6).

Rainforest vitality is known to depend on rainfall amount and dry season length (2, 7–9), but major knowledge gaps remain regarding rainforest influences on wet season onset. Rainforest evapotranspiration (ET) accounts for ∼30–50% of regional rainfall (10–13), but it is unclear whether ET actively modifies or merely responds to rainfall seasonality. Credible assessments of land use contributions to recent increases in dry season length and the frequency of extreme droughts in this region (14, 15) require these gaps to be filled.

## The Deep Convection Moisture Pump

Wet season onset in the tropics is generally associated with either monsoon reversals in the land–ocean temperature gradient or north–south migration of the Intertropical Convergence Zone (ITCZ), both of which are driven by seasonal changes in the distribution of solar radiation. However, wet season onset over the southern Amazon precedes the southward migration of the Atlantic ITCZ by ∼2–3 mo (16) and occurs without a reversal in the land–ocean surface temperature gradient (17, 18). Conventional mechanisms therefore cannot explain wet season onset over the southern Amazon. An alternative hypothesis holds that late dry season increases in rainforest transpiration may increase surface air humidity and buoyancy (18, 19). Lifting of this humid near-surface air by cold fronts moving northward from midlatitude South America (20) could cause large-scale increases in deep convection and upper-level heating (21), thereby initiating moisture transport from the tropical Atlantic. Large-scale moisture transport reinforces the conditions that favor deep convection, ultimately leading to wet season onset. We refer to this transition mechanism as the deep convective moisture pump (DCMP).

The exact processes that activate the DCMP have been unclear. Cold front incursions are strongest during the dry season (22), but deep convection is rare until lower tropospheric humidity rises late in the transition season (21). Moistening of the lowest 4 km of the atmosphere (pressures $\gtrsim$600–700 hPa) therefore emerges as the likely key to activating the DCMP (23, 24). The source of this moisture and the processes by which moistening occurs have profound implications for understanding how land use and biomass burning affect the seasonal cycle of rainfall. For example, deforestation might sharpen the land–ocean temperature gradient (accelerating wet season onset under a conventional onset mechanism), but would also reduce surface moisture fluxes (delaying wet season onset under an ET-initiated onset mechanism).

To clarify the mechanisms involved in activating the DCMP, the first question that must be answered is whether the late dry season increase in lower tropospheric humidity primarily derives from rainforest transpiration or advection from the ocean. Previous studies on this topic have been overwhelmingly based on reanalysis products that combine available observations

### Significance

This analysis provides compelling observational evidence that rainforest transpiration during the late dry season plays a central role in initiating the dry-to-wet season transition over the southern Amazon. Transpiration first activates shallow convection that preconditions the atmosphere for regional-scale deep convection, rather than directly activating deep convection as previously proposed. Isotopic fingerprints in atmospheric moisture unequivocally identify rainforest transpiration as the primary moisture source for shallow convection during the transition. This "shallow convection moisture pump" thus depends on high transpiration rates during the late dry season, affirming the potential for climate and land use changes to alter or disrupt wet season onset in this region.

Author contributions: R.F. designed research; J.S.W. performed research; J.S.W., J.R.W., S.C., N.E.C., C.R., Y.S., and L.Y. analyzed data; and J.S.W. and R.F. wrote the paper.

The authors declare no conflict of interest.

This article is a PNAS Direct Submission.

[1]To whom correspondence should be addressed. Email: rfu@atmos.ucla.edu.

[2]Present address: School of Integrative Plant Science, Soil and Crop Sciences Section, Cornell University, Ithaca, NY 14853.

This article contains supporting information online at www.pnas.org/lookup/suppl/doi:10.1073/pnas.1621516114/-/DCSupplemental.

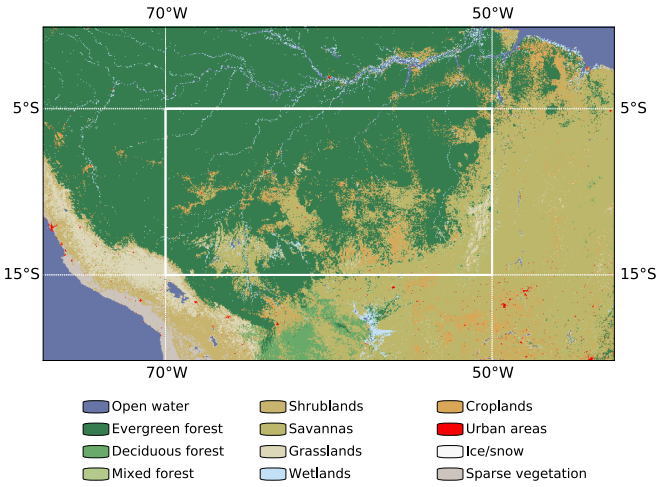


**Fig. 1.** Distribution of land cover based on Moderate-Resolution Imaging Spectroradiometer observations from 2009. The southern Amazon (5°S to 15°S, 50°W to 70°W) is indicated by the solid white box.

with numerical model simulations. These products are heavily influenced by the behavior of the underlying model in data-poor regions like Amazonia. Inadequate treatments of surface hydrology, vegetation, and turbulent mixing near the top of the atmospheric boundary layer (ABL) lead to large uncertainties in reanalysis estimates of ET, rainfall, and moisture flux convergence (MFC) (25). For example, the increase in rainfall over the southern Amazon during the dry-to-wet season transition occurs ∼2–3 wk earlier in the European Center for Medium-Range Weather Forecasting Interim Reanalysis (ERA-Interim) than in observations (*SI Text*). Enhanced rainfall and associated heating in the atmosphere directly affect reanalysis estimates of ET and MFC, potentially confounding moisture source attributions based on reanalysis products. In situ observations indicate that maximum ET leads the late dry season increase in rainfall (26–28); however, it has been unclear whether modest increases in ET can contribute sufficient moisture above the ABL at regional scales. The potential influences of aerosols on the dry-to-wet season transition are an additional source of uncertainty (29), because the aerosol climatologies used by most reanalyses neglect or underestimate seasonal and interannual variations in aerosol loading in this region (30, 31). It is therefore necessary to examine the dry-to-wet season transition by using observable quantities.

## Stages of the Dry-to-Wet Season Transition

Fig. 2 shows the evolution of atmospheric, land surface, and vegetation properties over the southern Amazon during the transition season. Reanalysis ET and MFC are included for context; all other quantities are derived from satellite observations. Each time series is a sequence of 5-d means composited relative to wet season onset (day 0; *Materials and Methods*). Negative times indicate days before wet season onset. Wet season onset typically occurs in middle October over the southern Amazon. Specific onset dates are listed in Table S1.

We divide the transition season into three stages: a pretransition (90–60 d before onset), an early transition (60–30 d before onset), and a late transition (30–0 d before onset). The pretransition stage marks a turning point from seasonal drying to seasonal moistening. This turning point is reflected in column water vapor (CWV; Fig. 2*C*), but does not emerge in precipitation until the following stage (Fig. 2*A*). Surface air temperature (Fig. 2*C*) and reanalysis sensible heating (Fig. S1) increase during the pretransition, consistent with a brief rise in absorbed surface

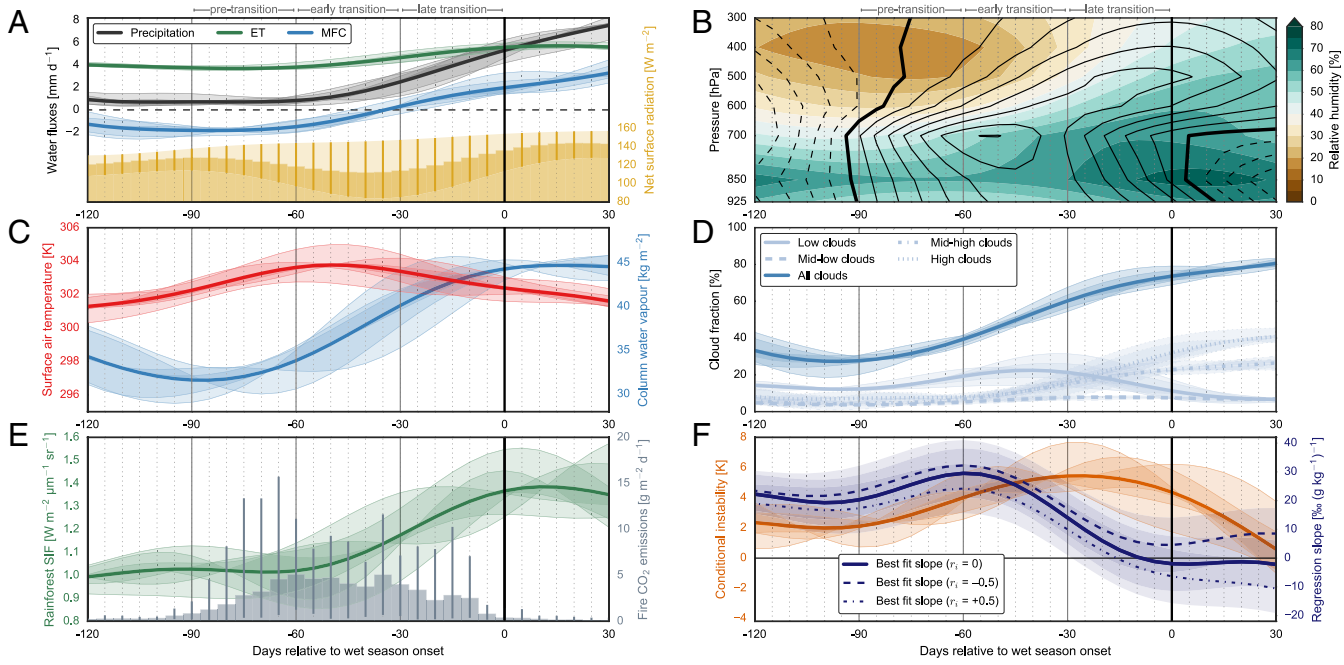


**Fig. 2.** Onset-relative low-pass filtered composites of area mean precipitation from Tropical Rainfall Measuring Mission (TRMM), ET and MFC from ERA-Interim, and net absorbed surface radiation from Clouds and the Earth's Radiant Energy System (CERES) Synoptic Radiative Fluxes and Clouds (SYN1Deg) (*A*); vertical distributions of RH (shading) and time rates of change in equivalent potential temperature ($\partial\theta_e/\partial t$; contour interval 0.02 K d$^{-1}$) computed from Atmospheric Infrared Sounder (AIRS) observations (*B*); surface air temperature and column water vapor (CWV) from AIRS (*C*); low (<700 hPa; ∼3 km above sea level), midlow (700–500 hPa; ∼3–5.5 km), midhigh (500–300 hPa; ∼5.5–10 km), high (>300 hPa; ∼10 km), and total cloud cover from CERES SYN1deg (*D*); solar-induced chlorophyll fluorescence (SIF) for rainforests from the Global Ozone Monitoring Instrument 2 and fire emissions of $CO_2$ from Version 3.1 of the Global Fire Emissions Database (*E*); conditional instability in the lower–middle troposphere ($\theta_{e850} - \theta_{e500}$) based on AIRS and best-fit linear slopes of $\delta$D against specific humidity ($q$) in the free troposphere based on TES (*F*). Shaded areas in *A* and *C*–*F* and error bars in *A* and *E* illustrate estimated uncertainties. Data sources, quality control criteria, and uncertainty calculations are provided in *SI Text*.

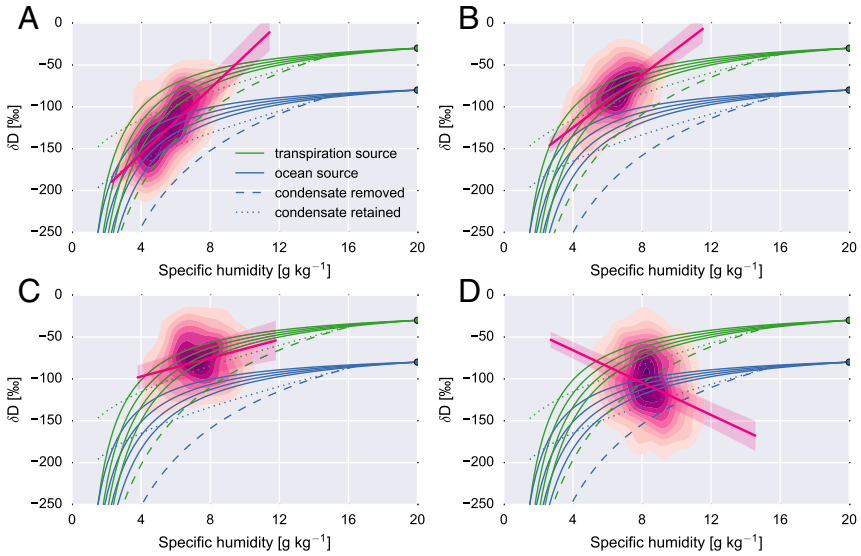


**Fig. 3.** Joint distributions of specific humidity ($q$) and the deuterium content of water vapor ($\delta$D) in the lower troposphere (825–600 hPa) based on TES observations during the pretransition stage (day −90 to −60) (*A*), early transition (day −60 to −30) (*B*), late transition (day −30 to 0) (*C*), and the first 3 mo of the wet season (day 0 to +90) (*D*). The joint behaviors of $q$ and $\delta$D under three types of idealized vertical mixing are also shown. Solid green and blue lines represent mixing (no condensation) between four dry air masses representing the dry season free troposphere and a moist air mass representing either local ET (green; $q = 20$ g kg$^{-1}$; $\delta$D = −30‰) or ocean evaporation (blue; $q = 20$ g kg$^{-1}$; $\delta$D = −80‰). Dashed green and blue lines represent pseudoadiabatic Rayleigh distillation from the approximate top of the ABL, in which condensation occurs in a rising air parcel and is immediately removed as precipitation. Dotted green and blue lines represent reversible moist adiabatic ascent from the approximate top of the ABL, in which condensation occurs and is assumed to remain in the parcel. These idealized models are described in detail in *SI Text*.

radiation (Fig. 2*A*) that often reverses as aerosol loading increases (see also Fig. S2). Changes in the vertical profile of relative humidity (RH) suggest that enhanced sensible heating deepens the daytime ABL, mixing dry free tropospheric air into the ABL and moist ABL air into the free troposphere (Fig. 2*B*). Increases in low cloud cover (Fig. 2*D*) also imply ABL growth and more frequent shallow cumulus. Biomass burning emissions increase during this phase (Fig. 2*E*), consistent with dry conditions.

Several important changes in moist thermodynamics and atmospheric stability begin during the pretransition. Contours in Fig. 2*B* show the time rate of change in equivalent potential temperature ($\theta_e$), a measure of moist entropy. Decreases in $\theta_e$ with height indicate conditional instability, under which convection may be triggered if condensation occurs in the lower troposphere. We quantify conditional instability as the difference in $\theta_e$ between 850 hPa, slightly above the ABL top, and 500 hPa, in the middle troposphere (Fig. 2*F*). Larger positive values indicate greater potential for moist convection to occur. Positive $\partial\theta_e/\partial t$ in the lower troposphere after day −90 causes conditional instability to grow. Positive changes in $\theta_e$ can arise from net warming (via diabatic heating or thermal advection) or moistening (via upward or lateral moisture transport). The lower tropospheric winds are divergent over almost the entire southern Amazon during the pretransition stage, with net exports of both heat and moisture (Fig. 2*A*). Increases in lower tropospheric $\theta_e$ must therefore arise from local processes, such as latent and radiative heating associated with low clouds, upward mixing of moist air in shallow convection, or radiative heating due to aerosols.

The early transition is characterized by increases in rainfall and rainforest photosynthesis, along with continued destabilization of the atmosphere. Surface air temperature (Fig. 2*C*) plateaus, but shallow convection intensifies, as indicated by strong positive $\partial\theta_e/\partial t$ within the lower troposphere (Fig. 2*B*) and continued increases in low cloud cover (Fig. 2*D*). Conditional instability continues to grow (Fig. 2*F*), as increases in convective available potential energy (CAPE) and decreases in convective inhibition confirm the development of an increasingly favorable environment for convection (Fig. S3). Moistening accelerates in the lower troposphere and begins to penetrate into the upper troposphere (Fig. 2 *B* and *C*). We infer rainforest photosynthesis and plant transpiration from SIF, which scales with gross primary productivity (32). SIF increases from approximately day −60 (Fig. 2*E*), broadly consistent with the evolution of reanalysis ET (Fig. 2*A*) and other satellite-derived vegetation indices (Fig. S4). The increase in reanalysis ET between days −60 and −30 (~1 mm·d$^{-1}$; Fig. 2*A*), which is similar in magnitude to observed increases in ET (27), can account for most of the early transition increase in rainfall (~1.5 mm·d$^{-1}$).

The late transition marks a shift from shallow to deep convection. The center of increasing $\theta_e$ moves upward from the lower middle troposphere (near 700 hPa) to the upper middle troposphere (near 500 hPa). The advent of regional-scale deep convection drives continued increases in precipitation (Fig. 2*A*), but halts and then reverses the trend in conditional instability (Fig. 2*F*). The evolution of conditional instability may be understood as follows. Shallow convection during the pretransition and early transition transports moist entropy to the lower troposphere, increasing conditional instability and eroding the thermodynamic barrier to deep convection. Deep convection during the late transition consumes conditional instability and converts its underlying potential energy into the kinetic energy of the monsoon circulation (21). Temperature changes play an important role in increasing lower tropospheric $\theta_e$ during the pretransition, but most of the early transition increase is due to rising humidity (Fig. S5). We therefore refer to this process as the shallow convection moisture pump (SCMP). SIF, enhanced vegetation index, and ET continue to increase during the late transition. Increases in ET between day −30 and onset (<1 mm·d$^{-1}$) account for less than a third of the rise in rainrate (~3 mm·d$^{-1}$), implying that late-transition increases in RH and deep convection are primarily fueled by large-scale moisture convergence.

## Water Vapor and its Isotopic Composition

The moisture source analysis discussed above references reanalysis estimates of ET and MFC, which may be unduly influenced by biases in the model-generated background state. We therefore supplement this analysis by examining the isotopic content

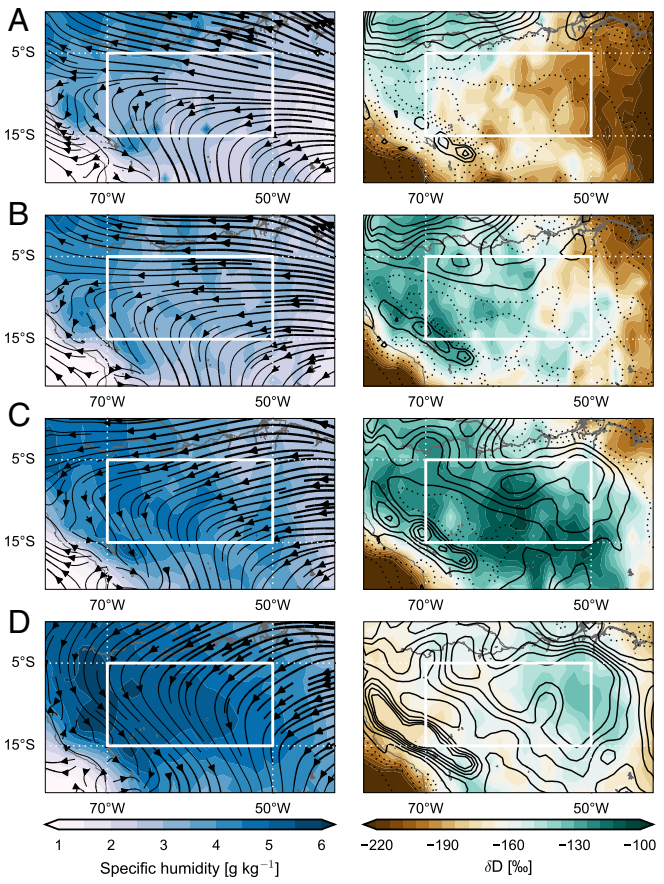


**Fig. 4.** Distribution of specific humidity (*Left*) and $\delta$D (*Right*) in the free troposphere based on TES observations during the pretransition (day −90 to −60) (*A*), early transition (day −60 to −30) (*B*), late transition (day −30 to 0) (*C*), and early wet season (day 0 to +90) (*D*). Winds at 850 hPa (*Left*) and vertically integrated MFC (*Right*) based on ERA-Interim are also shown for each stage of the transition. The contour interval for MFC is 1 kg m$^{-2}$ d$^{-1}$.

of water vapor. Stable water isotopes are valuable tracers of the origin and history of air masses. Molecular differences among common isotopes (such as $H_2{}^{16}O$ and HDO) cause fractionation during most phase transitions: Heavier isotopes (HDO) preferentially condense, whereas lighter isotopes ($H_2{}^{16}O$) preferentially evaporate (33). Evaporation from the ocean surface and condensation during transport both deplete the deuterium content of water vapor relative to its source. By contrast, no fractionation occurs during steady-state transpiration, so that the mean isotopic composition of transpired vapor is virtually identical to that of soil water (34, 35). Here, we evaluate the joint evolution of water vapor and its deuterium content ($\delta$D; *Materials and Methods*) in the free troposphere (750–348 hPa) over the southern Amazon using satellite observations (36).

The atmosphere over the southern Amazon has two main moisture sources: rainforest ET and ocean evaporation (10). Under thermodynamic equilibrium conditions, $\delta$D in tropical ocean evaporate has an isotopic composition of approximately −70 to −80‰. Estimating the isotopic composition of soil water as that of local rainfall (*SI Text*), $\delta$D for rainforest ET is approximately −20 to −40‰ (Fig. S6). We can therefore treat ocean evaporation and rainforest ET as isotopically distinct moisture sources, with rainforest ET relatively enriched in deuterium. If free tropospheric moistening is dominated by upward mixing of local ET, then the largest specific humidities in the free troposphere will be associated with the highest values of $\delta$D. If moistening is instead dominated by transport from oceanic sources, then the larger specific humidities will be associated with lower values of $\delta$D. The evolution of moisture sources in the free troposphere over the southern Amazon can therefore be diagnosed by using linear fits of $\delta$D against specific humidity ($q$). These linear fits have larger positive slopes when the primary moisture source is upward mixing of ET, and smaller or negative slopes when the primary moisture source is large-scale transport.

Fig. 3 shows distributions of TES measurements of lower tropospheric $q$ and $\delta$D during the three stages of the transition and the first 90 d of the wet season. Joint variations of $q$ and $\delta$D predicted by several theoretical models are also shown for context. These theoretical models are organized into two groups. The first group (green lines) corresponds to a local ET moisture source ($\delta$D = −30‰). The second group (blue lines) corresponds to an ocean evaporation moisture source ($\delta$D = −80‰). The models correspond to dry mixing, reversible moist adiabatic ascent, and Rayleigh distillation (33, 37). The dry mixing model represents intermixing of two air masses without condensation, whereas the other two models track the evolution of a single undilute air parcel undergoing lifting and condensation (see *SI Text* for details).

During the pretransition (Fig. 3*A*), the peak of the joint distribution based on TES observations matches expectations for the subtropical free troposphere: dry air with low $\delta$D descending from the upper troposphere mixed with air rising from the tropical ocean ABL (33). However, the distribution also contains a moist tail that is highly enriched in deuterium and can only be explained by upward mixing of local ET. The $q$-$\delta$D slope during the pretransition is large and positive, as expected for the case in which moistening is dominated by upward mixing of transpired water vapor. The entire distribution shifts upward and toward the right during the early transition (Fig. 3*B*), indicating moister air with larger $\delta$D. This distribution, which corresponds to the peak activity of the SCMP (Fig. 2*B*), is consistent with a dominant local ET moisture source. The $q$–$\delta$D slope for this stage remains large and positive, but is slightly reduced from the pretransition because dry, depleted observations are less common. The center of the distribution during the late transition is similar to that during the early transition, but with an increased

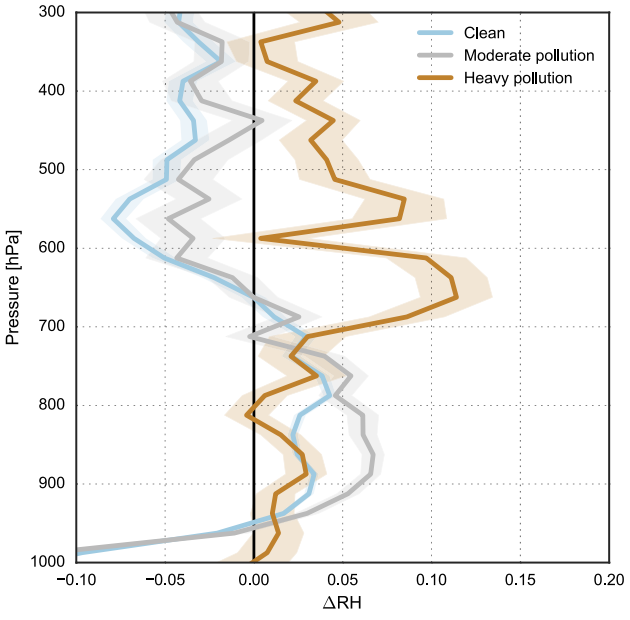


**Fig. 5.** Changes in the vertical profiles of RH (ΔRH) associated with shallow convection under clean conditions [Cloud condensation number concentrations (CCN) ≤ 500 cm$^{-3}$], moderate aerosol pollution (500 cm$^{-3}$ < CCN ≤ 1,000 cm$^{-3}$), and heavy aerosol pollution (CCN > 1,000 cm$^{-3}$). CCN, RH profiles, and convective occurrence are based on observations collected during the Green Ocean Amazon (GOAmazon) field campaign (*SI Text*). ΔRH is reported in absolute differences.

prevalence of moist air with low δD (Fig. 3*C*). This shift is consistent with enhanced MFC (more vapor from the nearby ocean; Fig. 2*A*) and more frequent deep convection (more distillation of heavy isotopes via convective precipitation; Fig. 2 *B* and *D*), and results in a substantially reduced $q$–δD slope relative to the early transition. The moist, low-δD tail of the late-transition distribution becomes the center of the distribution during the wet season (Fig. 3*D*). The wet season $q$–δD slope is negative due to repeated distillation of free tropospheric vapor by deep convection (33, 38). The onset-relative evolution of $q$–δD slopes over the southern Amazon (Fig. 2*F*) can thus be understood as a trajectory in the $q$–δD phase space (Fig. 3) that traces three paradigms in sequence: dry/depleted through moist/enriched to moist/depleted.

Spatial distributions of water vapor and δD in the free troposphere (Fig. 4) provide additional context. During the pretransition, large values of $q$ and δD are limited to the heavily forested northwestern corner of the domain (Fig. 4*A*). Moist, deuterium-enriched air then spreads south and east across the domain as area mean precipitation increases (Fig. 4 *B* and *C*). This propagation broadly matches the northwest-to-southeast migration of wet season onset (39). The spatial gradient of δD reverses during the wet season (Fig. 4*D*), when deuterium-rich water vapor is located in the northeast, close to the ocean, but water vapor concentrations are largest in the west. These wet season distributions are consistent with transport from the tropical Atlantic feeding regional-scale deep convection, which keeps the free troposphere moist but depleted of deuterium. The transition to an oceanic moisture source and the removal of deuterium in convective rainfall both contribute to the wet season anticorrelation between $q$ and δD. Wet season onset typically occurs latest over the northeastern corner of the domain (39). Colocated maxima in δD and MFC (Fig. 4 *C* and *D*) suggest that onset there relies on large-scale moisture convergence forced by deep convective heating, as opposed to the ET-driven onset that prevails over most of the domain.

## SCMP

Rain-generating deep convective storms occur in this region when CWV, RH, and $\theta_e$ are larger than normal, particularly in the lower–middle troposphere (24). Area mean changes in the moist thermodynamic properties of the atmosphere (Fig. 2) indicate that the SCMP acts to establish these conditions over the southern Amazon ∼30 d before wet season onset. To demonstrate that these regional-scale changes are consistent with the influences of individual shallow convective events, we evaluate changes in the vertical profile of RH associated with shallow convection during the transition season. Because convection in this region is influenced by aerosol loading (29), we examine these changes separately for shallow convection during clean, moderate, and heavily polluted conditions (Fig. 5).

An increase in RH in the lower troposphere (950–700 hPa, 0.5∼3 km above sea level) is observed after shallow convection occurs under clean and moderate conditions. Moderate aerosol loading appears to slightly enhance the lower-tropospheric moistening associated with shallow convection, perhaps due to aerosol-induced reductions in precipitation efficiency that favor longer cloud lifetimes (40, 41). Shallow convective moistening is shifted upward under heavy pollution, reflecting upward displacements of cloud base and cloud top in a systematically drier atmosphere. These results, based on instantaneous measurements, establish the capacity of the SCMP to increase lower tropospheric RH during the early stages of the transition season, a key precondition for subsequent increases in deep convection. Our interpretations of aerosol effects are speculative, but highlight the potential influences of biomass burning on the SCMP and the need for further study.

## Implications

The fate of the southern Amazon rainforest depends on the length of the dry season (2, 4). Here, we have shown that the length of the dry season in this region also depends on the rainforest. Rainforest ET during the late dry season helps to initiate a chain of atmospheric processes that hastens wet season onset 2–3 mo before the arrival of the ITCZ. This finding bolsters the hypothesis that deforestation could delay onset and lengthen the dry season (3). Given the importance of the rainforest-mediated SCMP and the strong sensitivity of shallow convection to land cover in this region (42), the dry-to-wet transition may be more sensitive to land use and vegetation changes than previously thought. Many models remain unable to realistically represent rainforest ET and shallow convection (43, 44), leading to misdiagnosis of the mechanisms that control wet season onset and large discrepancies in projected climate changes over the southern Amazon (45). A more detailed understanding of the water isotopic budget would provide valuable constraints for model evaluation and development.

Variations in the timing of wet season onset are often attributed to large-scale climate patterns like the El Niño–Southern Oscillation and the Atlantic Multidecadal Oscillation (46), but the mechanisms by which oceanic conditions during March–May influence wet season onset and forest fire activity in the southern Amazon during August–October are unclear (47, 48). Our results imply that reduced deep soil moisture recharge during March–May associated with El Niño or warmer conditions in the tropical North Atlantic could delay onset by suppressing rainforest ET during August–October (the early transition season). ET-initiated wet season onset mechanisms may also apply in other parts of the Amazon, but further investigation would be needed to evaluate this possibility.

## Materials and Methods

All analyzed fields are area-weighted spatial averages over the southern Amazon domain, defined as the area bounded by 5°S to 15°S and 50°W to 70°W (Fig. 1). Variables are averaged into discrete 5-d periods (pentads) starting each year from 1 to 5 January. The annual cycle of each variable is composited relative to wet season onset for each individual year following Li and Fu (19). Onset dates are listed in Table S1. Onset-relative composites are constructed by averaging across years for the 81 5-d periods centered on onset over multiple wet season transitions (2007–2008 through 2013–2014 for SIF; 2005–2006 through 2010–2011 for all other variables). Composite time series are then filtered using fast Fourier transforms to remove variability at time scales shorter than 25 d (Fig. S7).

The deuterium content of water vapor is expressed as the relative ratio δD in parts per thousand (‰), where

$$\delta\mathrm{D} = 1000 \times \left(\frac{R - R_{\mathrm{std}}}{R_{\mathrm{std}}}\right). \quad [1]$$

$R$ is the ratio of the number of HDO molecules to the number of $H_2O$ molecules and $R_{\mathrm{std}}$ is the corresponding ratio in Vienna Standard Mean Ocean Water ($R_{\mathrm{std}} = 3.11 \times 10^{-4}$). Joint distributions of specific humidity ($q$) and δD are based on retrievals from the Tropospheric Emission Spectrometer (TES) on the EOS Aura satellite (49); see *SI Text* and Figs. S8 and S9 for additional details on these retrievals. Linear fits of δD on $q$ account for residuals and uncertainties in both variables (50). Detailed descriptions of data sources, quality control criteria, uncertainty calculations, theoretical models, and potential confounding factors are provided in *SI Text*.

**ACKNOWLEDGMENTS.** This work was supported by a Young Thousand Talents fellowship and National Natural Sciences Foundation of China Research Fund for International Young Scientists (Grant 41350110225) at Tsinghua University; along with National Science Foundation Grant AGS-0937400; NASA Aura Science Team Program Grant NNX09AD85G; the Department of Energy GOAmazon Project; and NASA Earth and Space Science Fellowship Program Grant NNX13AN95H. Part of the research described in this paper was carried out by the Jet Propulsion Laboratory, California Institute of Technology, under a contract with NASA.

1. Field CB, Behrenfeld MJ, Randerson JT, Falkowski P (1998) Primary production of the biosphere: Integrating terrestrial and oceanic components. *Science* 281(5374): 237–240.

2. Staver AC, Archibald S, Levin SA (2011) The global extent and determinants of savanna and forest as alternative biome states. *Science* 334(6053): 230–232.

3. Fu R, et al. (2013) Increased dry-season length over southern Amazonia in recent decades and its implication for future climate projection. *Proc Natl Acad Sci USA* 110(45):18110–18115.
4. Oyama MD, Nobre CA (2003) A new climate-vegetation equilibrium state for Tropical South America. *Geophys Res Lett* 30(23):2199.
5. Gash JHC, Nobre CA (1997) Climatic effects of Amazonian deforestation: Some results from ABRACOS. *Bull Am Meteorol Soc* 78:823–830.
6. Berbery EH, Barros VR (2002) The hydrologic cycle of the La Plata basin in South America. *J Hydrometeor* 3(6):630–645.
7. Marengo JA (1992) Interannual variability of surface climate in the Amazon Basin. *Int J Climatol* 12:853–863.
8. Hutyra LR, et al. (2005) Climatic variability and vegetation vulnerability in Amazônia. *Geophys Res Lett* 32(24):L24712.
9. Guan K, et al. (2015) Photosynthetic seasonality of global tropical forests constrained by hydroclimate. *Nat Geosci* 8(4):284–289.
10. Salati E, Dall'Olio A, Matsui E, Gat JR (1979) Recycling of water in the Amazon Basin: An isotopic study. *Water Resour Res* 15(5):1250–1258.
11. Eltahir EAB, Bras RL (1994) Precipitation recycling in the Amazon basin. *Q J R Meteorol Soc* 120(518):861–880.
12. van der Ent RJ, Savenije HHG, Schaefli B, Steele-Dunne SC (2010) Origin and fate of atmospheric moisture over continents. *Water Resour Res* 46(9):W09525.
13. Dirmeyer PA, Wei J, Bosilovich MG, Mocko DM (2014) Comparing evaporative sources of terrestrial precipitation and their extremes in MERRA using relative entropy. *J Hydrometeorol* 15(1):102–116.
14. Davidson EA, et al. (2012) The Amazon basin in transition. *Nature* 481(7381):321–328.
15. Escobar H (2015) Drought triggers alarms in Brazil's biggest metropolis. *Science* 347(6224):812.
16. Fu R, Arias PA, Wang H (2016) The connection between the North and South American monsoons. *The Monsoons and Climate Change: Observations and Modeling*, eds de Carvalho LMV, Jones C (Springer International, Cham, Switzerland), pp 187–206.
17. Lenters JD, Cook KH (1995) Simulation and diagnosis of the regional summertime precipitation climatology of South America. *J Clim* 8(12):2988–3005.
18. Fu R, Zhu B, Dickinson RE (1999) How do atmosphere and land surface influence seasonal changes of convection in the tropical Amazon? *J Clim* 12:1306–1321.
19. Li W, Fu R (2004) Transition of the large-scale atmospheric and land surface conditions from the dry to the wet season over Amazonia as diagnosed by the ECMWF re-analysis. *J Clim* 17:2637–2651.
20. Siqueira JR, Rossow WB, Machado LAT, Pearl C (2005) Structural characteristics of convective systems over South America related to cold-frontal incursions. *Mon Weather Rev* 133:1045–1064.
21. Li W, Fu R (2006) Influence of cold air intrusions on the wet season onset over Amazonia. *J Clim* 19:257–275.
22. Garreaud RD, Wallace JM (1998) Summertime incursions of midlatitude air into subtropical and tropical South America. *Mon Weather Rev* 126:2713–2733.
23. Mapes BE, Tulich S, Lin J, Zuidema P (2006) The mesoscale convection life cycle: Building block or prototype for large-scale tropical waves? *Dyn Atmos Ocean* 42:3–29.
24. Schiro KA, Neelin JD, Adams DK, Lintner BR (2016) Deep convection and column water vapor over tropical land versus tropical ocean: A comparison between the Amazon and the tropical western Pacific. *J Atmos Sci* 73(10):4043–4063.
25. Fernandes K, Fu R, Betts AK (2008) How well does the ERA40 surface water budget compare to observations in the Amazon River basin? *J Geophys Res Atmos* 113(D11):D11117.
26. da Rocha HR, et al. (2004) Seasonality of water and heat fluxes over a tropical forest in eastern Amazonia. *Ecol Appl* 14:22–32.
27. Juárez RIN, Hodnett MG, Fu R, Goulden ML, von Randow C (2007) Control of dry season evapotranspiration over the Amazonian forest as inferred from observations at a Southern Amazon forest site. *J Clim* 20(12):2827–2839.
28. Hasler N, Avissar R (2007) What controls evapotranspiration in the Amazon basin? *J Hydrometeorol* 8(3):380–395.
29. Rickenbach TM, Nieto-Ferreira R, Barnhill RP, Nesbitt SW (2011) Regional contrast of mesoscale convective system structure prior to and during monsoon onset across South America. *J Clim* 24(14):3753–3763.
30. Tegen I, et al. (1997) Contribution of different aerosol species to the global aerosol extinction optical thickness: Estimates from model results. *J Geophys Res Atmos* 102:23895–23915.
31. Colarco P, da Silva A, Chin M, Diehl T (2010) Online simulations of global aerosol distributions in the NASA GEOS-4 model and comparisons to satellite and ground-based aerosol optical depth. *J Geophys Res* 115:D14207.
32. Joiner J, et al. (2013) Global monitoring of terrestrial chlorophyll fluorescence from moderate-spectral-resolution near-infrared satellite measurements: Methodology, simulations, and application to GOME-2. *Atmos Meas Tech* 6(10):2803–2823.
33. Galewsky J, et al. (2016) Stable isotopes in atmospheric water vapor and applications to the hydrologic cycle. *Rev Geophys* 54:809–865.
34. McGuffie K, Henderson-Sellers A (2004) Stable water isotope characterization of human and natural impacts on land-atmosphere exchanges in the Amazon Basin. *J Geophys Res* 109(D17):D17104.
35. Farquhar GD, Cernusak LA, Barnes B (2007) Heavy water fractionation during transpiration. *Plant Physiol* 143(1):11–18.
36. Worden J, et al. (2012) Profiles of CH4, HDO, H2O, and N2O with improved lower tropospheric vertical resolution from Aura TES radiances. *Atmos Meas Tech* 5(2): 397–411.
37. Noone D (2012) Pairing measurements of the water vapor isotope ratio with humidity to deduce atmospheric moistening and dehydration in the tropical midtroposphere. *J Clim* 25(13):4476–4494.
38. Worden J, Noone D, Bowman K (2007) Importance of rain evaporation and continental convection in the tropical water cycle. *Nature* 445(7127):528–532.
39. Marengo JA, Liebmann B, Kousky VE, Filizola NP, Wainer IC (2001) Onset and end of the rainy season in the Brazilian Amazon Basin. *J Clim* 14:833–852.
40. Albrecht BA (1989) Aerosols, cloud microphysics, and fractional cloudiness. *Science* 245(4923):1227–1230.
41. Ackerman AS, Kirkpatrick MP, Stevens DE, Toon OB (2004) The impact of humidity above stratiform clouds on indirect aerosol climate forcing. *Nature* 432(7020): 1014–1017.
42. Heiblum RH, Koren I, Feingold G (2014) On the link between Amazonian forest properties and shallow cumulus cloud fields. *Atmos Chem Phys* 14(12):6063–6074.
43. Nam C, Bony S, Dufresne J-L, Chepfer H (2012) The 'too few, too bright' tropical low-cloud problem in CMIP5 models. *Geophys Res Lett* 39(21):L21801.
44. Wu J, et al. (2016) Leaf development and demography explain photosynthetic seasonality in Amazon evergreen forests. *Science* 351(6276):972–976.
45. Yin L, Fu R, Shevliakova E, Dickinson RE (2013) How well can CMIP5 simulate precipitation and its controlling processes over tropical South America? *Clim Dyn* 41(11-12):3127–3143.
46. Liebmann B, Marengo JA (2001) Interannual variability of the rainy season and rainfall in the Brazilian Amazon basin. *J Clim* 14:4308–4318.
47. Chen Y, Velicogna I, Famiglietti JS, Randerson JT (2013) Satellite observations of terrestrial water storage provide early warning information about drought and fire season severity in the Amazon. *J Geophys Res Biogeosci* 118(2):495–504.
48. Yin L, et al. (2014) What controls the interannual variation of the wet season onsets over the Amazon? *J Geophys ResAtmos* 119(5):2314–2328.
49. Worden J, et al. (2006) Tropospheric Emission Spectrometer observations of the tropospheric HDO/H2O ratio: Estimation approach and characterization. *J Geophys Res* 111(D16):D16309.
50. York D, Evensen NM, Martínez ML, Delgado JDB (2004) Unified equations for the slope, intercept, and standard errors of the best straight line. *Am J Phys* 72(3): 367–375.
51. Huffman GJ, et al. (2007) The TRMM Multisatellite Precipitation Analysis (TMPA): Quasi-global, multiyear, combined-sensor precipitation estimates at fine scales. *J Hydrometeorol* 8(1):38–55.
52. Dee DP, et al. (2011) The ERA-Interim reanalysis: Configuration and performance of the data assimilation system. *Quart J R Meteorol Soc* 137:553–597.
53. Wielicki BA, et al. (1996) Clouds and the Earth's radiant energy system (CERES): An Earth observing system experiment. *Bull Am Meteorol Soc* 77(5):853–868.
54. Kato S, et al. (2013) Surface irradiances consistent with CERES-derived top-of-atmosphere shortwave and longwave irradiances. *J Clim* 26(9):2719–2740.
55. Minnis P, et al. (2011) CERES Edition-2 cloud property retrievals using TRMM VIRS and Terra and Aqua MODIS data—Part I: Algorithms. *IEEE Trans Geosci Remote Sens* 49(11):4374–4400.
56. Doelling DR, et al. (2013) Geostationary enhanced temporal interpolation for CERES flux products. *J Atmos Ocean Tech* 30(6):1072–1090.
57. Bloom S, da Silva A, Dee D (2005) *Documentation and Validation of the Goddard Earth Observing System (GEOS) Data Assimilation System-Version 4* (National Aeronautics and Space Administration, Greenbelt, MD), Tech Rep. NASA/TM-2005-104606/VOL26/VER4.
58. Rienecker MM, et al. (2008) *The GEOS-5 Data Assimilation System - Documentation of Versions 5.0.1, 5.1.0, and 5.2.0*, (National Aeronautics and Space Administration, Greenbelt, MD), Tech Rep. NASA/TM-2008-104606-VOL-27.
59. Huete A, et al. (2002) Overview of the radiometric and biophysical performance of the MODIS vegetation indices. *Remote Sens Environ* 83(1):195–213.
60. van der Werf GR, et al. (2010) Global fire emissions and the contribution of deforestation, savanna, forest, agricultural, and peat fires (1997–2009). *Atmos Chem Phys* 10(23):11707–11735.
61. Mu M, et al. (2011) Daily and 3-hourly variability in global fire emissions and consequences for atmospheric model predictions of carbon monoxide. *J Geophys Res Atmos* 116(D24):D24303.
62. Olsen ET, et al. (2013) *AIRS/AMSU/HSB Version 6 Data Release User Guide*, (Jet Propulsion Laboratory, Pasadena, California), Tech Rep.
63. Tian B, et al. (2013) *AIRS/amsu/hsb version 6 level 3 product user Guide* (Jet Propulsion Laboratory, Pasadena, CA), Tech Rep.
64. Williams E, Renno N (1993) An analysis of the conditional instability of the tropical atmosphere. *Mon Weather Rev* 121:21–36.
65. York D (1966) Least-squares fitting of a straight line. *Can J Phys* 44:1079–1086.
66. York D (1969) Least squares fitting of a straight line with correlated errors. *Earth Planet Sci Lett* 5:320–324.
67. Wehr R, Saleska SR (2017) The long-solved problem of the best-fit straight line: Application to isotopic mixing lines. *Biogeosciences* 14(1):17–29.
68. Field RD, Jones DBA, Brown DP (2010) Effects of postcondensation exchange on the isotopic composition of water in the atmosphere. *J Geophys Res Atmos* 115(D24):D24305.
69. Dansgaard W (1964) Stable isotopes in precipitation. *Tellus* 16(4):436–468.
70. Brooks RJ, Barnard HR, Coulombe R, McDonnell JJ (2009) Ecohydrologic separation of water between trees and streams in a Mediterranean climate. *Nat Geosci* 3(2): 100–104.
71. Jouzel J (1986) Isotopes in cloud physics: Multistep and multistage processes. *Handbook of Environmental Geochemistry* The Terrestrial Environment B, eds Fritz P, Frontes JC (Elsevier, New York), Vol 2, pp 61–112.
72. Majoube M (1971) Fractionnement en oxygene-18 et en deuterium entre l'eau et sa vapeur. *J Chim Phys* 68:1423–1436.